ATMOSPHERIC HETEROGENEITIES FROM ERS TANDEM SAR INTERFEROMETRY AND SEA SURFACE IMAGES

R.F. Hanssen

Delft Institute for Earth-Oriented Space Research,
Delft University of Technology, P.O. Box 5030
2600 GA Delft, The Netherlands
hanssen@geo.tudelft.nl

S. Lehner, I. Weinreich

Deutsches Zentrum für Luft- und Raumfahrt (DLR) e.V.
Oberpfaffenhofen
D-82234 Wessling, Germany
Susanne.Lehner@dlr.de, Ilona.Weinreich@dlr.de

Proceedings of the CEOS SAR workshop, 3-6 February 1998, ESTEC, Noordwijk, The Netherlands

Abstract

Lately it has been shown that interferograms from repeat pass SAR interferometry can show severe phase variation due to atmospheric heterogeneities. The effect is due to a differential time delay of the radar signal depending on spatial variations in the refractive index, caused by e.g. atmospheric water vapor variability.

In this paper the atmospheric features derived from the sea surface are used to explain the interferometric phase variation. Two adjacent ERS SAR tandem pairs centered over Flevoland in the Netherlands were used to derive a combined interferogram. The phase variation is discussed and compared to the meteorological situation using ground truth measurements and SAR derived wind speed and direction from the IJsselmeer.

The effects observed in both SAR backscatter from water surfaces and in the interferometric phase of the two combined SAR images are due to atmospheric boundary layer rolls. In-situ synoptic observations support the hypothesis that both backscatter and phase features have the same driving mechanism.

1. INTRODUCTION

Spaceborne SAR transforms its pulse returns into a complex vector for every imaged resolution cell. The intensity of this radar backscatter vector yields information on the roughness of the imaged surface. The argument of the vector is inherently random, due to the coherent superposition of the many different scatterers within a resolution cell. In an interferometric setting, however, the complex product of corresponding resolution cells in two images yields coherent path length differences caused by topography [5], deformation [7] and differential atmospheric delay [6], depending on the interferometric configuration.

The delay of the radar signal is caused by the integration over the refractive index of the propagation medium, along the line of sight. Horizontal and vertical heterogeneities in refractive index are influenced by the spatial distribution of water vapor, pressure, temperature, and liquid water [2].

The backscatter intensity over water surfaces is dominated by Bragg scattering. Contrasts in surface roughness can be interpreted as differences in wave height and air-sea interaction. Wind and rain are the main atmospheric phenomena which influence this intensity. Since the distribution of e.g. water vapor is strongly correlated with wind fields and convectivity, the same atmospheric phenomena may be identified in the intensity images as well as in the interferometric phase observations, as long as they continue over land. The ESA scatterometer algorithm CMOD4 can be used to derive wind speed from calibrated ERS SAR images of the sea surface, the direction of the wind is needed as additional input. This is usually derived from wind streaks in the SAR image.

In this study, we compare observed wind streaks over water areas in the backscatter intensity images with wave effects observed in the interferograms over the land areas. The study area covers a large part of the Netherlands, including the IJsselmeer lake area, and is centered approximately over the Flevoland polder. In section 2 we describe the interferometric analysis and interpretation, followed by the backscatter intensity analysis in section 3. Section 4 describes the meteorological information used as ground truth. In the last section, conclusions on the observed effects are drawn.

2. INTERFEROMETRIC PHASE ANALYSIS

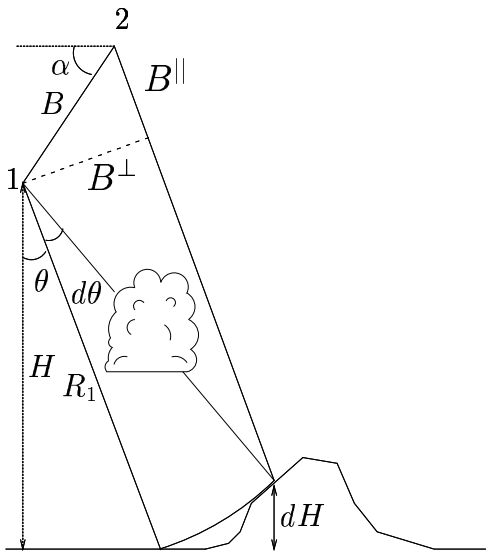

Figure 1: The interferometric configuration with a localized inhomogeneity

Figure 1 sketches the repeat pass interferometric configuration with two satellites at positions 1 and 2 with baseline B. Assuming full correlation between the two images, the influence of a localized increase in refractivity, indicated by the cloud symbol, is an excess distance ΔR_i in one of the two phase measurements ψ_i:

$$\psi_1 = \frac{4\pi}{\lambda}(R_1 + \Delta R_1) \quad (1)$$

$$\psi_2 = \frac{4\pi}{\lambda}(R_1 + B^{||} + \Delta R_2) \quad (2)$$

where $\lambda = 5.66$ cm is the wavelength of the ERS SAR, and $B^{||}$ is the parallel baseline. In the interferometric phase φ, both phase observations are differenced, which results in

$$\varphi = \frac{4\pi}{\lambda}(-B^{||} + \Delta R_1 - \Delta R_2). \quad (3)$$

Using some trigonometry and (3), horizontal differences in interferometric phase, $d\varphi$, can now be described by

$$d\varphi = \frac{4\pi}{\lambda}\left(\frac{B^{\perp}}{R_1 \sin\theta} dH + d\Delta R_1 - d\Delta R_2\right), \quad (4)$$

where $B^{\perp}$ is the perpendicular baseline, R_1 is the slant range to a pixel from satellite 1, and θ is the look angle. Knowing the topographic height variation dH, the first component within the braces can be eliminated, leaving only horizontal gradients in the atmospheric delay $d\Delta R_i$, either during the first image acquisition, yielding a positive sign, or during the second acquisition which yields a negative sign.

Equation (4) shows that the influence of localized signal delays on the interferometric phase is *not* related to the perpendicular baseline, in contrary to topographic height.

2.1. Interferometric processing

Two consecutive SAR frames (# 1035 and 1053) were acquired in orbit 24566 of ERS-1 and 4893 of ERS-2 at 26.03.96 and 27.03.96 at 21:40 UTC. The differential interferogram shown in figure 2 is obtained by the elimination of the topographic phase using an a-priori elevation model. For the lower right corner of the interferogram, indicated by the line in figure 2, no topographic data are available. This area is excluded from further analysis. The original unwrapped interferogram shows a strong increase of 2 phase cycles in the southern image, see [2]. Whether this is either a processing artifact, or a long wavelength atmospheric water vapor gradient, the ramp is removed using a polynomial best-fit since it is not of interest for the current work.

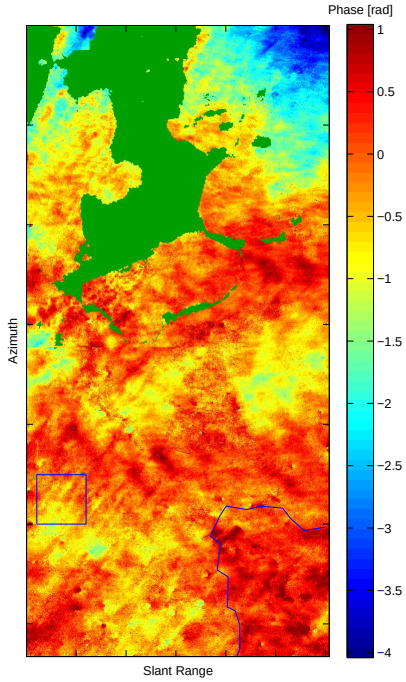

Figure 2: The unwrapped differential interferogram, covering an area of approximately 100×200 km. The square indicates the position of the wave effects in the interferometric phase.

Phase variation with a limited amplitude is apparent in the whole image, although highest fluctuation occurs in the upper parts of the interferogram. Local areas, within a square of 25 km, have a rms value of 0.36–0.68 rad. The area of interest for this study is indicated by the square in figure 2, where diagonal

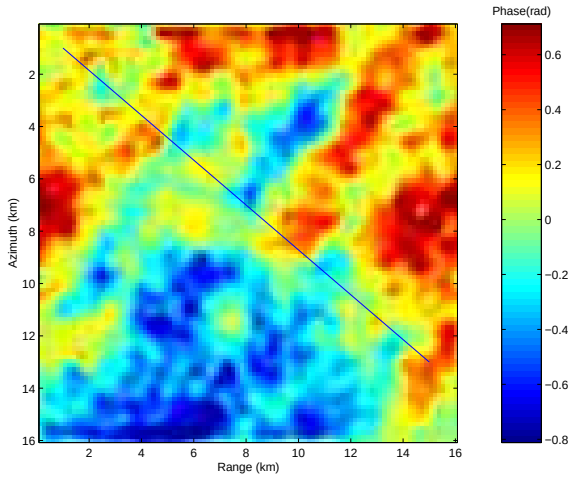

Figure 3: The highlighted extraction from the differential interferogram in figure 2.

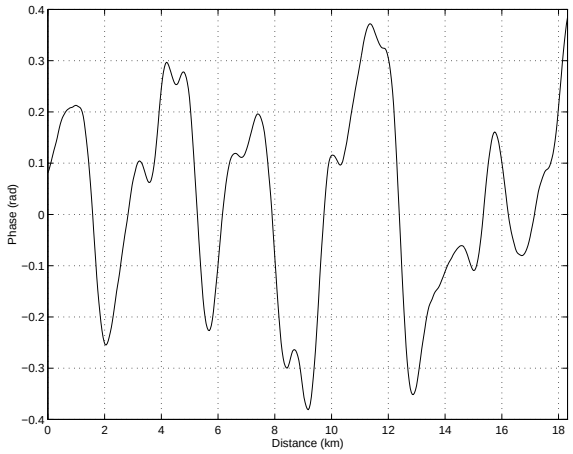

Figure 4: The cross section shown by the line in figure 3, perpendicular to the main direction of the features.

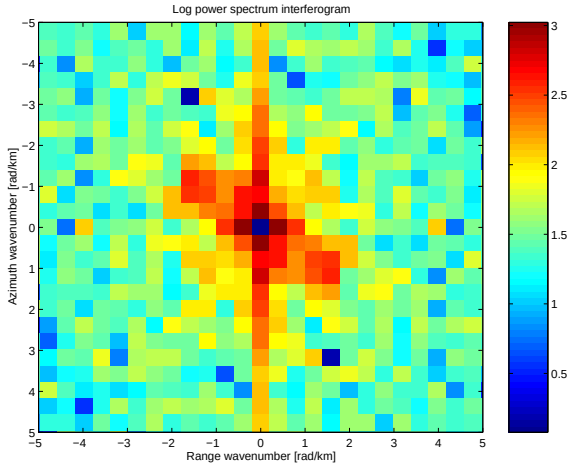

Figure 5: Two dimensional spectrum of the interferogram extraction shown in figure 5

linear waves can be observed. The waves are found within an area of 50×50 km.

Figure 3 shows a zoom of the indicated square from the differential interferogram in figure 2. Low pass filtering has been applied to suppress noise and some phase unwrapping artifacts. A cross section is indicated by the straight line in figure 3, and plotted in figure 4. It shows a maximal amplitude of approximately 0.6 rad, which corresponds to 3 mm one way zenith delay.

Figure 5 shows the two-dimensional power spectrum. The longitudinal direction of the waves can be found from the location of the side peaks in the spectrum, and is 34 ± 4 degrees with respect to the azimuth direction, which translates to 21 ± 4 degrees with respect to the north. The dominant wavelength is approximately 3.5 km.

3. BACKSCATTER INTENSITY ANALYSIS

Figures 6 and 7 show the intensity of the ERS SAR images (frame 1053) from March 26 (orbit 24566) and March 27 (orbit 04893) respectively. In the March 26 image, wind streaks can be detected on the IJsselmeer. It is immediately obvious that they have approximately the same direction as the waves in the interferogram. The synoptic observations (see Section 4) state a low wind speed (less than 2 m/s) on March 27. Therefore we can exclude the presence of wind streaks in that SAR scene.

Figure 6: ERS-1 SAR: 26.3.96 21:40:57 UTC

To compare the direction of the wind streaks with the waves in the interferogram and the synoptic wind

Figure 7: ERS-2 SAR: 27.3.96 21:40:56 UTC

measurements, the wind direction is determined—with a 180 degree ambiguity—from the power spectrum, see figure 8. Using this information together

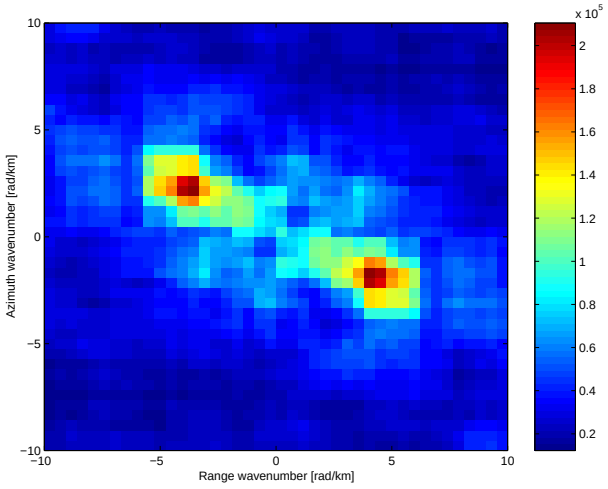

Figure 8: Power spectrum of wind streaks in IJsselmeer, 26.3.96, 21:40:57 UTC

with the wind shadowing behind the eastern coast, a wind direction of 23 ± 5 degrees with respect to north is derived.

Since the SAR is working at the same wavelength as the scatterometer, wind speed can be derived by the same algorithm as the scatterometer signal (CMOD4, [9]). To determine wind speed the normalized radar backscatter cross-section (NRCS) of the ERS SAR image is derived using the respective calibration procedures [4], [8]. Using the wind direction as stated above the wind speed is determined using CMOD4, resulting in 5.1 m/sec. A second alternative method for deriving wind speed is used for comparison. In this approach [3] the width of the azimuthal cross correlation function of two looks of the SAR image is used to determine mean orbital velocity movement of the water surface. This in turn is a measure of wind speed. With this algorithm we obtain 5.4 m/s which agrees quite well with CMOD4.

4. METEOROLOGICAL OBSERVATIONS

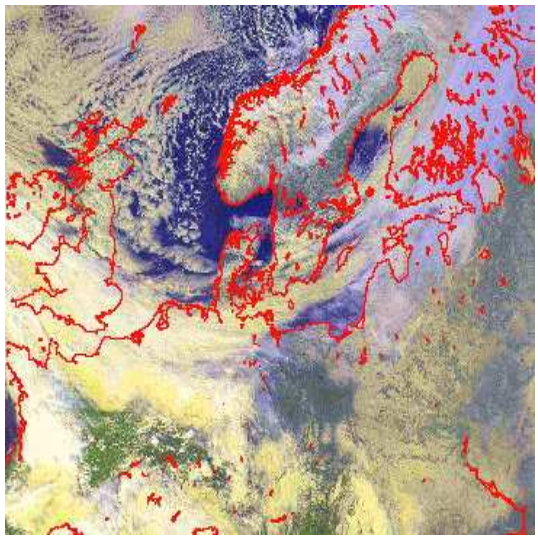

Figure 9: NOAA-14 AVHRR: 26.3.96 11:58 UTC

The surface weather maps of March 26 and 27, 1996 show that a weak low over central Europe moved southward, and a weak cold front was progressing from the north southward over the Netherlands. Advanced Very High Resolution Radiometer (AVHRR) images in figure 9 and 10, acquired at noon, show the progression of this cold front.

At the time of the March 26 SAR acquisition, the cold front has already passed by. During the passage of the front there are several cloud layers, middle to higher level, there is no precipitation and there is advection of cold air, according to synoptic observations. Near the occurrence of the waves in the interferogram, there is 3/8 cloud coverage of stratocumulus at 1000 m, and 7/8 stratocumulus at 1300 m. The temperature at 2 meters above the ground is around 2°C in the southern parts of the interferogram. Relative humidity is 69%, and wind speeds are around 7 m/s from 20 degrees with respect to the north.

At March 27, Meteosat infrared imagery indicates cold cirrus clouds over the North Sea. Cloud cover has moved towards the south, as observed by AVHRR in figure 10. The synoptic weather stations report only some high level cirrus clouds, which are

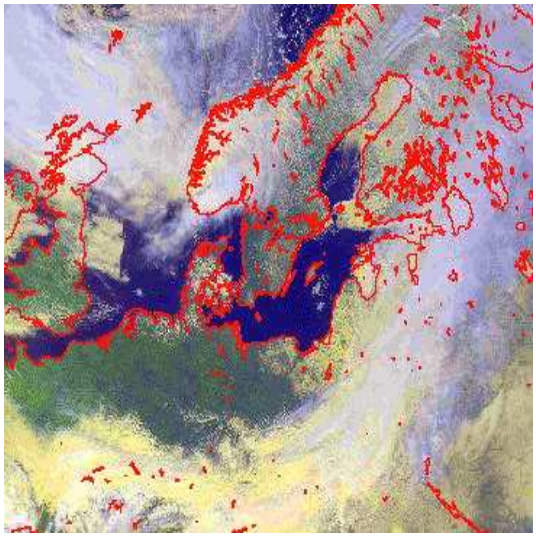

Figure 10: NOAA-14 AVHRR: 27.3.96 11:47 UTC

the first signs of a warm front entering the Netherlands at March 28. The temperature is just below the freezing level (−1°C) at 22:00 UTC. The relative humidity is 76%. Wind speeds are lower than 2 m/s coming from 0–20 degrees with respect to the north.

In figure 11, wind vectors obtained by synoptic observations are shown. The dashed line shows the coverage of the two SAR acquisitions. The length of the arrows is a measure for the wind speed. The

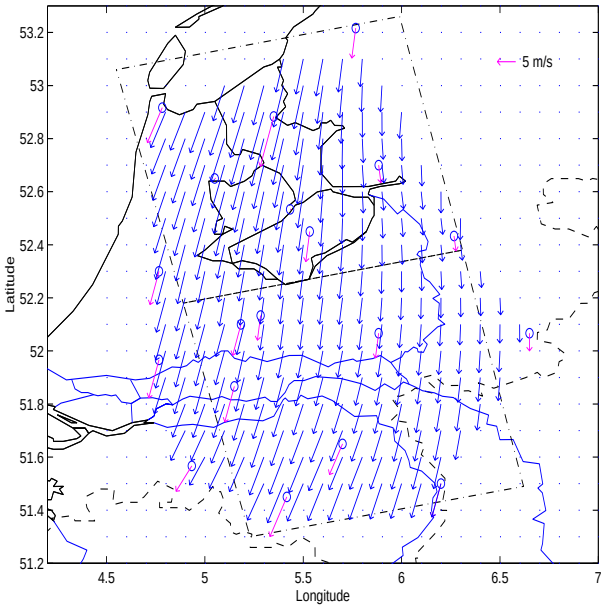

Figure 11: Wind field acquired by synoptic observations, 26.3.96, 22:00 UTC. The rectangles indicate the position of the SAR images. Purple vectors indicate the station observations.

figure shows how the wind slightly curves to the west at the south of the interferogram. Interpolated values for the studied water and land areas are given in table 1.

Figure 12 shows the radiosonde profile from station De Bilt at 18:00 UTC. From the wind direction and velocity *barbs* it is clear that between 1600 and 4000 m, the wind direction has changed from 15 degrees to 285 degrees. At higher altitudes, the prevailing wind direction is west. The close distance between the dew-point curve and the temperature reveals a high relative humidity in the boundary layer. Vertical lines indicate the liquid water potential temperature, There is a strong inversion at 1200 m, and a second one at 2400 m.

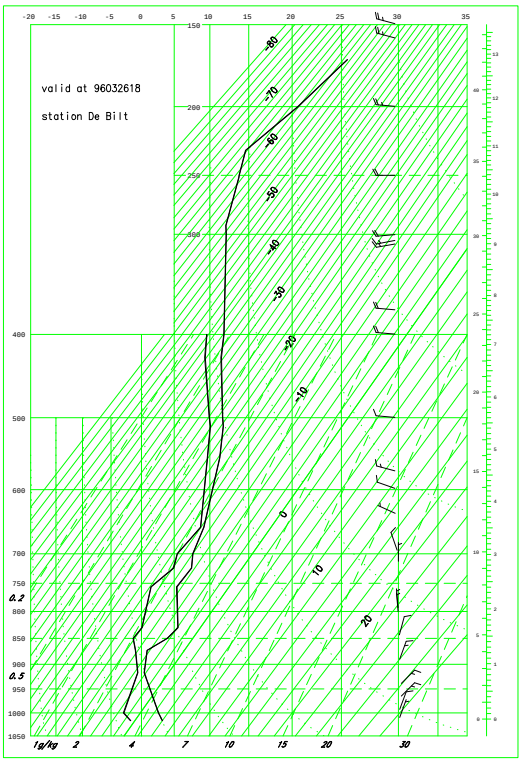

Figure 12: The radiosonde profile of station De Bilt, 26.03.96, 18:00 UTC

5. DISCUSSION

Table 1 shows the observations in the interferogram and the backscatter images as well as the synoptic measurements. As the synoptic measurements are acquired just before the hour, there is a time interval of approximately 15 minutes between the SAR measurements. Furthermore, the synoptic wind direction and velocity values are obtained over the study areas using linear interpolation. The wavelength of the wind streaks and interferometric wave patterns are only observed in the SAR and INSAR images. In the

Table 1: Wind observations for March 26, 1996, synoptic data 22:00 UTC, SAR data 21:40 UTC

	Direction [deg]	Velocity [m/s]	Wavelength [km]	Amplitude [mm]
Synoptic (water)	16 ± 5	7.3 ± 0.5	—	—
SAR backscatter (CMOD4)	23 ± 5	5.1 ± 2.0	1.4 ± 0.2	—
(Az. corr.)		5.4 ± 2.0		—
INSAR phase	21 ± 4	—	3.5 ± 0.2	2–3
Synoptic (land)	19 ± 5	6.8 ± 0.5	—	—

interferometric observation, the phase amplitude of the waves yield also a one-way zenith delay, given in millimeters.

The observed wind speeds from the backscatter images and the synoptic measurements are in relatively good agreement. The wind streaks in the SAR backscatter image, figure 6, and the waves in the interferogram, figure 2, have the same direction but differ in wavelength by a factor two. We assume that the doubling of the wavelength from the SAR image to the interferogram is caused by variations in effective wind speed induced by the wind rolls. The effective wind speed is the sum of the main geostrophic wind and a secondary component, perpendicular to the main wind. This perpendicular wind results in alternating convergent and divergent wind zones. The effective wind speed has a minimum at the divergence as well as the convergence centers and a maximum in between. This implies that there are two minima (at convergence and divergence) and two maxima (in between) for every observed wave in the interferogram.

As the temperatures at the SAR acquisitions are low, the relatively warm water of the IJsselmeer warms the air in the breeze over it. Due to this warming, it can contain more moisture, and small convective processes start, resulting in wind rolls. Over land these processes continue, although the cold land surface will cool the air again, resulting in an increase in relative humidity, and possibly condensation. This condensation in combination with the rolls can possibly lead to cloud streets. First SAR observations of changes in wind speed related to cloud streets were given for SEASAT by [1]. An exact comparison to the wavelength was not possible so far.

Previous research on horizontal convective rolls indicated that the roll updrafts were more moist than the roll downdraft regions throughout the entire convective boundary layer [10]. This phenomenon results in spatial "streets" of increased humidity, which are observed with SAR interferometry.

6. CONCLUSIONS

SAR backscatter information over water areas can be used to obtain information on wind direction and velocity. Interferometric repeat pass SAR is impossible over water due to temporal decorrelation, but is able to detect spatial variations in the refractive index over land. Therefore, in SAR imagery containing water as well as land areas, both techniques can be regarded complementary for the analysis of atmospheric dynamics, such as boundary layer rolls or possibly rain fields.

Prior knowledge of potential atmospheric signal in SAR interferograms can be a selection criterion to find the most suitable interferometric combination to reduce errors in e.g. topographic mapping. This study shows that the information from the backscatter over water areas can give indications on the atmospheric disturbance in the interferograms.

Whereas conventional SAR backscatter analysis has proved capable of deriving wind velocities and detecting wave phenomena over water areas at the surface, analysis of the interferometric phase yields measures of the amplitude of the water content in the atmosphere in the whole return path, in terms of integrated signal delay. This quantity can be connected with atmospheric water vapor distribution or converted into precipitable water, and give more insight in dynamic atmospheric processes at water-land boundaries.

ACKNOWLEDGEMENT

The ERS SAR images were kindly provided by ESA. Part of the work was funded by the German Ministry of Research (BMBF) under contract number 03F0165C.

References

[1] T. W. Gerling. Structure of the surface wind field from SEASAT SAR. *J. Geophys. Res.*, 91:2308–2320, 1986.

[2] R. F. Hanssen. Assessment of the role of atmospheric heterogeneities in ERS tandem SAR interferometry. Technical report, Delft Institute for Earth-Oriented Space Research, Delft, the Netherlands, 1998. Final report for the European Space Agency. In print.

[3] V. Kerbaol and B. Chapron. Calibration and validation of ERS-1/2 wave mode products, 1996. Report to the European Space Agency under PO NO 160709.

[4] S. Lehner, J. Horstmann, W. Koch, and W. Rosenthal. Mesoscale wind measurements using recalibrated ERS SAR images. *J. Geophys. Res.*, 1998. In print.

[5] F. K. Li and R. M. Goldstein. Studies of multibaseline spaceborne interferometric synthetic aperture radars. *IEEE Trans. on Geoscience and Remote Sensing*, 28(1):88–97, January 1990.

[6] D. Massonnet and K. L. Feigl. Discrimination of geophysical phenomena in satellite radar interferograms. *Geophysical Research Letters*, 22(12):1537–1540, 1995.

[7] D. Massonnet, M. Rossi, C. Carmona, F. Adagna, G. Peltzer, K. Feigl, and T. Rabaute. The displacement field of the Landers earthquake mapped by radar interferometry. *Nature*, 364(8):138–142, July-8 1993.

[8] P.J. Meadows, H. Laur, and J.I. Sanchez. The ERS SAR performances. In *this issue*, 1998.

[9] A. Stoffelen and D. L. T. Anderson. Wind retrieval and ERS-1 scatterometer radar backscatter measurements. In *World Space Congress, Washington*, 1992.

[10] T.M. Weckwerth, J.W. Wilson, and R.M. Wakimoto. Thermodynamic variability within the convective boundary layer due to horizontal convective rolls. *Monthly Weather Review*, 124:769–784, 1996.